



Experimental investigation of masonry building damage caused by surface tension cracks on slow-moving landslides

Qin Chen^{1,2} · Lixia Chen³ · Renato Macciotta² · Kunlong Yin¹ · Lei Gui¹ · Yu Zhao³ · Yingxue Liao³

Received: 24 March 2022 / Accepted: 11 August 2023 / Published online: 4 September 2023
© The Author(s), under exclusive licence to Springer Nature B.V. 2023

Abstract

Slow-moving landslides cause significant economic losses associated with damage to facilities and interruption of human activity in mountainous regions and along river valleys. Physical vulnerability of structures exposed to slow-moving landslides is a required input for informed risk mitigation decision-making. However, the quantification of this vulnerability is still a major challenge. Few studies have been completed on this topic due to the limited historical data of the building damage associated with the comprehensive descriptions of the landslide mechanism. This research presents an experimental approach to investigating the mechanism of damage development and evolution on masonry buildings exposed to ground tension cracks associated with slow-moving landslides. A one-tenth scale model of a masonry building was designed and tested on the newly developed test table. The details of the testing setup are presented in this paper. The scaled model was constructed using sintered clay brick masonry and an unreinforced concrete foundation. An artificial tension crack was opened under the scaled model through the application of loading steps, in the direction parallel to the model foundation. The internal strains and associated forces developed on the scale model walls and foundation were measured by strain gauges. It was observed that the damage ranged from cracking to partial out-of-plane failure of the walls and the foundation. The damage level increased with the propagation of the tension crack on the test table. The final observation results were compared and validated against the field observations of damaged buildings on slow-moving landslides in TGR area in China. The experimental loading device simulated building damage caused by ground horizontal displacements and can bridge the gap in understanding the effects of slow-moving landslides on structures. It provided a new way to analyze the vulnerability of masonry structure under horizontal movement patterns of slow-moving landslides.

Keywords Building damage · Ground tension crack · Loading device · Masonry structure · Physical model test · Slow-moving landslide · Vulnerability

Abbreviations

TGR Three gorges reservoir
DInSAR Differential interferometric synthetic aperture radar
InSAR Interferometry with satellite radars with synthetic aperture

| | |
|------|------------------------------------|
| GNSS | Global navigation satellite system |
| UAV | Unmanned aerial vehicle |

Symbols

| | |
|---------------|--|
| σ | Stress of material (Pa) |
| ε | Strain of material |
| E | Young's modulus (Pa) |
| ν | Poisson's ratio |
| ρ | Mass density (kg/m^3) |
| l | Length (m) |
| δ | Linear movement (m) |
| θ | Angular movement (rad) |
| A | Area (m^2) |
| P | Concentrated load (N) |
| M | Moment (N m) |
| m | Mass (kg) |
| C | Cement |
| S | Sand |
| G | Stone |
| W | Water |
| F | The dimension of the force |
| L | The dimension of the length |
| T | The tractive force from the loading device |

1 Introduction

Slow-moving landslides are widely distributed all over the world (Mansour et al. 2011). Some examples can be found in Italy (Antronico et al. 2015; Ferlisi et al. 2019), Canada (Macciotta et al. 2016; Huntley et al. 2019), China (Jiang et al. 2020; Chen et al. 2020; Li et al. 2021), and the USA (Lowry et al. 2013; Sun et al. 2015). These landslides cause huge economic losses in terms of damage to facilities (buildings, infrastructure, etc.) (Abbaszadeh Shahri et al. 2019), interruption of human activities (Peduto et al. 2017; Ali et al. 2020; Kilicoglu et al. 2020; Woods et al. 2020, 2021), and transportation corridors (Journault et al. 2018; Carlà et al. 2018; Deane et al. 2020; Rodriguez et al. 2021).

Deformation of slow-moving landslides directly causes physical damages to buildings and is one of the important parameters on vulnerability quantification. Structures with high vulnerability are common on the boundaries of sliding, or in the tension zones (Fell 2018). The deformation positions on the slow-moving landslides (e.g., near the toe, the crown, and the boundary) and mechanical characteristics (e.g., tension, shearing, and extrusion) should be considered in detail. The quantitative method should be proposed for vulnerability of buildings under the different ground surface deformation. Therefore, at first, it is necessary to understand the damaging effect and the deformed mechanism of the buildings which is damaged by the ground surface cracks on slow-moving landslides.

However, quantitative physical vulnerability is still a major challenge because of limited damage records and unclear damaging effect of buildings. Most research on physical vulnerability of buildings focus on the effect of fast-moving landslides. Few researchers focus on the effects of slow-moving landslides (Mansour 2009; Carlà et al. 2018; Mavrouli et al.

2019; Ferlisi et al. 2021). Therefore, data of slow-moving landslide on building damages are limited now and not enough for analysis by statistical method, which is current commonly adopted for vulnerability assessments (e.g., Galli and Guzzetti 2007; Uzielli et al. 2015; Kang and Kim 2016). Especially for landslides along the bank of the Three Gorges Reservoir (TGR) in China, there are few publicly-available records on the effects of slow-moving landslides on buildings to allow a statistical evaluation.

To enrich the data on physical vulnerability, many researchers employ the data from remote sensing and numerical models associated with slow-moving landslide displacement and building deformation. Differential Interferometric Synthetic Aperture Radar (DInSAR) is a commonly adopted remote sensing technique (Cascini et al. 2010; Ferlisi et al. 2015; Peduto et al. 2017). The numerical modeling approaches adopted include the Equivalent Frame Method (Nicodemo et al. 2020) and the Finite element approach (Sangirardi et al. 2020). These studies aimed to analyze the damage evolution of masonry buildings interacting with slow-moving landslides. However, not all landslides have available adequate satellite imagery (e.g., dense vegetation, unfavorable slope orientation to the satellite line of sight), and numerical simulations require calibration to reduce uncertainty in input parameters and results.

Physical models provide a good method to overcome some of these above limitations and can be used for model calibration. Bothara et al. (2010) presented the results of an experimental test to investigate the seismic performance of a two-story brick masonry house with one room on each floor. Wu et al. (2011) developed an experimental setup to simulate the damage of buildings impacted by fast-moving landslides. Zhang et al. (2016a) developed a setup where a boulder could impact brick and concrete walls, allowing them to create the vulnerability function for such conditions. Yu et al. (2018) developed a calculation model for the maximum impact force imposed by a rock block on an object through simulations on physical models. But there are few experimental investigations focused on slow-moving landslides and the associated damage to buildings on these landslides.

Masonry structures are the most common types of residential building within the area of the TGR, China. The mechanism of masonry building damage caused by the slow-moving landslides is complex. Physical vulnerability factors include landslide deformation mechanisms (e.g., occurrence of tension, shearing, and extrusion), intensity characteristics (e.g., moving speed, thrust force, ground cracking widths, differential settlements), and structural characteristics of the buildings (e.g., type, geometry, foundation, expected deformation mode). These factors make it challenging to analyze the failure mechanism of masonry structures on slow-moving landslides. The work in this paper investigates the damage response of a model masonry structure effected by the development of tension cracks on slow-moving landslides.

During the evolution of slow-moving landslides, signs of deformation at the ground surface can become apparent, and are intensified as the slow movement continues. These landslide deformation features include tension cracks (e.g., those on the upper part of landslide, near the crest), shear cracks (e.g., those caused by overall sliding on the lateral edge of the landslide), and transverse or longitudinal cracks (e.g., those caused by extrusion on the lower part of landslide) (Xu et al 2008). Chen et al. (2016) found that the most sensitive indicator for building damage on slow-moving landslides was crack width. In particular, the ground tension cracks of the landslides have a serious impact on buildings and other infrastructures (Sangirardi et al 2020; Singh et al 2019; Macciotta et al 2017).

Focusing on the above factor, a physical experiment to investigate and analyze the response of masonry buildings as tension cracks develop on a typical slow-moving landslide was designed. The work in this paper investigates the damage response of a model

masonry structure affected by the development of tension cracks on slow-moving landslides. To this end, physical model tests were developed that will aid in developing a theoretical basis for studying the vulnerability of buildings to tension crack development on slow-moving landslides.

2 Slow-moving landslides in the TGR area and building damage caused by landslide tension cracks

According to the classification of landslide velocity (Cruden and Varnes 1996), the landslides moving between 0 and 16 mm/year are classified as extremely slow-moving landslides. Landslides moving at rates between 16 mm/year and 1.6 m/year are classified as very slow-moving landslides. Landslides moving at rates between 1.6 m/year and 13 m/month are classified as slow-moving landslides. 310 landslides have been mapped in the middle section of the TGR area (belonging to Chongqing). Satellite-based ground deformation measurements (Interferometry with satellite radars with synthetic aperture -InSAR) have been used on the area and 52 of the landslides were identified as active and in a slow-moving state (Liu et al. 2020). These landslides have been triggered by reservoir water level fluctuations, rainfall events, or a combination of these (Yang et al. 2019; Zhou et al. 2020; Du et al. 2020; Liang et al. 2021). Long-term slow displacements of these landslides have caused serious damage to the buildings in the area, particularly associated with tension cracks (Guo et al. 2020; Chen et al. 2016). This section presents some examples of reported damage in the TGR area.

2.1 Xiangjiaping landslide

The Xiangjiaping Landslide ($108^{\circ} 29' 33.20''$ E, $30^{\circ} 50' 16.25''$ N) is a translational landslide located on the south bank of the Yangtze River in the Wanzhou District of Chongqing. The landslide has a maximum length and width of 600 m and 550 m, respectively, covering a total area of approximately $33 \times 10^4 \text{ m}^2$, and with an estimated volume of $660 \times 10^4 \text{ m}^3$. The average depth of the sliding mass is 20 m. The slope angle of the landslide ranges between 11° and 15° . The exposed bedrock in the Xiangjiaping Landslide is from the mid-Jurassic Shaximiao group, consisting of burgundy mudstone, siltstone and sandstone, with main structures associated with bedding with a dip direction of 330 degrees and a dip angle of 5 degrees. The displaced material is composed of Quaternary loose deposits of silty clay with breccia, gravels, and rock blocks.

The landslide was triggered by the combined effect of reservoir water level fluctuation and rainfall (Du et al. 2018). Most deformation is concentrated at the front of the landslide, as shown in Fig. 1d. Seven GNSS (Global Navigation Satellite System) monitoring devices were installed on the lower and middle part of the Xiangjiaping landslide in 2016, one being a monitoring control point and the other six monitoring landslide displacements (Fig. 1a). Monitoring data shows that the accumulated displacements ranged between 29.3 and 283.9 mm between June 2016 and December 2020 (Fig. 1c). Monitoring stations WZ03 and WZ05 had the largest deformations at an average rate of approximately 5 mm/month. The accumulated displacements of other monitoring stations were significantly smaller. In general, The Xiangjiaping landslide showed a slow deformation pattern. Deformations along the left boundary and lower part of the landslide were faster than those in the middle and upper areas.

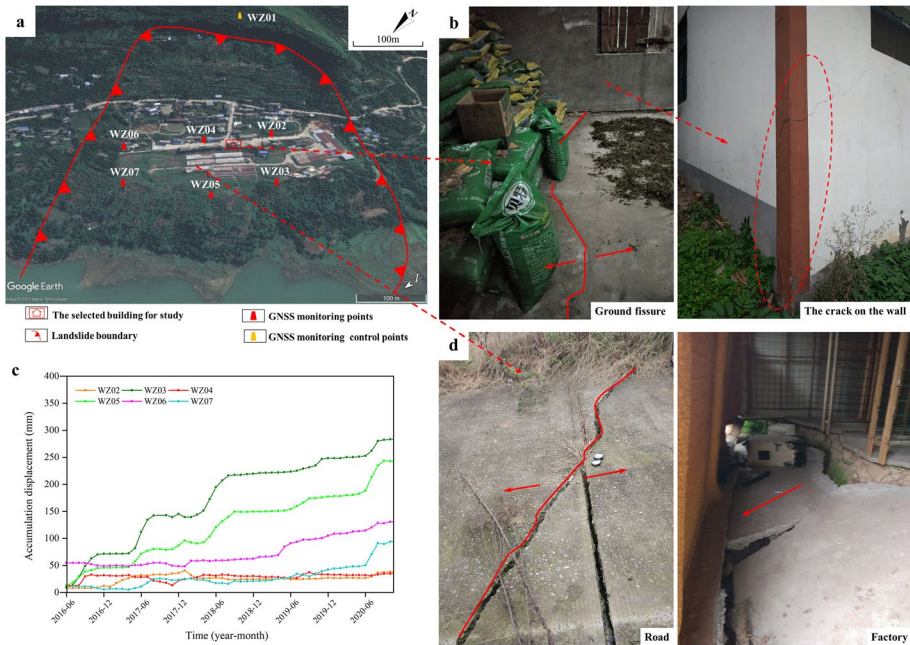


Fig. 1 Damage on masonry structure and road on the Xiangjiaping Landslide. **a** Google Earth image showing the landslide boundary and the location of the damaged building; **b** the ground crack of the damage building and the crack located in the corner of the wall. (taken in January 2019); **c** accumulated ground displacement of Xiangjiaping landslide obtained by GNSS monitoring (the monitoring data was provided by the Geological Environment Monitoring Master Station of Chongqing); **d** the deformation in the lower part of the Xiangjiaping landslide

The selected building for study is located mid-way within the area of the landslide showing the larger deformations. It is a one-story masonry structure. A surface crack developed through the building, paralleling to its longitudinal direction (Fig. 1b). The length and the maximum width of the surface crack were 14 m and 10 mm, respectively. It led to significant damage of the building walls. The crack on the wall extended from the transverse wall to the longitudinal wall along the corner which had a maximum length and width of about 4 m and 10 mm, respectively. Figure 1d also depicts ground fissures, road cracks, and significant differential settlements within the developed area on the landslide.

2.2 Lipingcun landslide

The Lipingcun landslide (108° 41' 55.58" E, 30° 34' 41.61" N) is located in the Wanzhou District of Chongqing. This landslide was triggered by rainfall on July 2, 2020. The landslide is fan-shaped and its main sliding direction is oriented at 240° from the North. The landslide elevation ranges between 820 and 875 m.a.s.l, with an average slope angle of approximately 20°. The toe of the landslide is adjacent to several residential buildings. It has an average thickness of 10 m and an estimated volume of $1.68 \times 10^4 \text{ m}^3$. The entire landslide involves an area of $16.8 \times 10^4 \text{ m}^2$, with a maximum longitudinal dimension of 120 m and an average width of 140 m (Fig. 2a). The landslide body mainly consists of



Fig. 2 Deformation on the Lipingcun Landslide and the damage of the building affected by surface crack C4. **a** unmanned aerial vehicle (UAV) image showing the landslide boundary (July, 2020); **b** surface tension crack C1; **c** surface tension crack C2. **d** Surface tension crack C3; **e** surface crack C4 traversing the building; **f** surface crack C4; **g** relative position of surface and wall cracks; **h** vertical wall crack; **i** crack on the corner of the wall; **j** cracks on internal walls

Quaternary deposits, including silty clay and fragmented rubble with a loose and disorderly structure. The lithology of the bedrock is mainly sandstone and mudstone of the Jurassic Shaximiao Formation, with a dip direction of 328° and dip of 9° .

In July 2020, the Lipingcun landslide experienced accelerated deformation rates triggered by heavy rainfall. Field investigation showed that there were tension cracks in the middle and upper part of the landslide with the maximum width of approximately 50 cm, and the depth of 120 cm (Table 1). The cracks were identified on July 2, 2020, and the width continued to increase on July 7, 2020 due to persistent rainfall (Fig. 2b–d and f). No monitoring equipment was set up so that no quantified displacement was available for this study. However, the observations on the tension cracks could be described.

Some residential houses suffered from severe damage due to the landslide deformation. The prototype of the physical model in the current study is chosen based on this building, which was located on the upper part of the area that showed the largest deformation based on the observed landslide features that developed during this event (Fig. 2a and e). The house was built in 2019 and was a one-story masonry structure with a length of 12 m and a width of 6 m. Witnesses (Local residents) indicated that the building was severely damaged in early July, 2020 and the deformation continued until July 17, 2020. This confirmed that the deformation of the building was synchronous with, and an effect of, the landslide event.

Surface tension crack C4, with a length 5.5 m, width of 10 cm, and maximum depth of 9 cm, severely damaged the walls, both in the transverse and longitudinal direction (Fig. 2f). A vertical crack on the wall was 106 cm distant from the ground crack (Fig. 2g). This vertical crack also occurred on the wall through its total height (floor to ceiling) with a length of approximately 3 m and maximum width of 2.5 cm (Fig. 2h). A diagonal crack (at 45° angle, following the mortar joining the bricks) was formed in a corner of the structure (Fig. 2i, j), rendering the corner of wall very fragile. It was observed in this and other structures that if a wall crosses a surface landslide tension crack, vertical cracks will develop on the wall near the surface landslide tension crack. The diagonal crack along the mortar joints appears to suggest weaker mortar on the corner of the structure and stress concentrations at the observed location. It is likely that the limited further deformation would have led to the collapse of the structure.

Controlling the potential consequences associated with slow-moving landslides interacting with masonry structures requires an improved understanding of the effect of surface cracks on structures such as those described above. A physical model experiment of a masonry structure subjected to landslide surface cracks was developed in order to better understand these effects.

Table 1 Characteristics of the surface cracks on the Lipingcun landslide

| No | Direction | Maximum crack length (m) | Maximum crack width (cm) | Maximum crack depth (cm) |
|----|-----------|--------------------------|--------------------------|--------------------------|
| C1 | 290°–300° | | 20 | 4–50 |
| C2 | 160° | | | 120 |
| C3 | 320° | | 50 | 20 |
| C4 | 175° | 5.5 | 8–10 | 9 |

3 Masonry structure model

3.1 Assumptions

The study aims at investigating the damage response of the masonry structure (common in the TGR area) affected by surface tensile cracks on slow-moving landslides. The following assumptions and simplifications were adopted:

- The model building is built on a steel plate with half fixed and half mobile plate. The displacement of the mobile steel plate models the width of a tensile crack on the ground surface.
- The ground tension crack is parallel to the longitudinal wall of the model building, which is placed across the center of the foundation.
- The settlement of the foundation bed is not considered. Differential settlements of different magnitudes are commonly observed, in our work we isolate this variable to evaluate the effects of the tensile component of landslide-induced deformations.
- The boundary effects between the foundation and the ground are not considered.

3.2 Theory of similarity and model design

The model has a geometric scale of $s_l = 1/10$. This resulted in a $1.2\text{m} \times 0.6\text{m}$ footprint of the model, and a height of 0.333m (Fig. 4). The width of the wall footing is 60 mm, with a depth of 50 mm. Scaled bricks had one of the bricks typically used in the area. The length, width, and height of the model bricks are 120 mm, 60 mm, and 30 mm (Fig. 3). To maintain a similar stress–strain curve between the model and the actual buildings, the same materials were used. The average compressive strength of the bricks was not less than 10 MPa.

Based on the Π theorem (Buckingham 1914), the quantities involved in the experiment follow the equations of the dimensional analysis applied to problems of stress and strain:

$$K_f = K_e K_l^2 = K_\sigma K_l^2 = K_\gamma K_l^3, \quad (1)$$

where K_f is the point load scale factor, K_e is the Young's modulus scale factor, K_l is the length scale factor, K_σ is the stress scale factor, and K_γ is the specific weight scale factor.

Because the material of the model and the real building is the same, $K_e = 1$ and $K_\sigma = 1$. Since the geometrical scale factor is $K_l = 1/10$, Eq. (1) accordingly yields $K_f = 1/100$, $K_\gamma =$

Fig. 3 The size of the model brick



10. Therefore, to reproduce the same stress field, the material specific weight of the model should be 10 times larger than the one of the prototype material. There are two possible strategies to overcome the problem: performing a centrifuge test, which induces an amplified acceleration on the structure, or introducing extra loads in the vertical direction, to reproduce the real stress gradient (Giardina et al. 2012). Due to the difficulty to replicate such a large and complex structure in a centrifuge, a total of 0.434 tonnes of additional mass was added to the walls of the model. We added the details in the manuscript. The similarity constant of the masonry structure model test is shown in Table 2.

3.3 Model fabrication

Most residential buildings in the mountain area of the TGR were built in the 1990s. These are generally one or two-story masonry structures, providing the rationale for selecting a masonry structure model with one story. This model aimed to represent a typical unreinforced masonry building in the TGR area. To reduce construction and interpretation complexity, no partition walls, doors, or windows were added.

Wall footings in the area are non-reinforced spread foundations, with typical buried depths (particularly the building used as example to design the model) between 0.3 and 0.5 m. Therefore, the model was built with a concrete strip footing, with a strength of C25 (the standard value of compressive strength is 25 ± 5 MPa), and adopt a concrete mix of 1:1.6:3.2:0.5 (cement: sand: stone: water). Table 3 shows the results of compressive strength and splitting tensile strength tests on the concrete used (Ministry of Housing and Urban–Rural Development of the PRC 2019).

The compressive strength tests were completed on the specimens of mortar with different proportions of water, cement, and aggregate (sand) (Table 4). The mortar cured for 3 days, 7 days, and 28 days (temperature of $20 \pm 2^\circ$ and relative humidity $\geq 90\%$) before testing (Ministry of Housing and Urban–Rural Development of the PRC 2009). According to the test data, the lower the cement content, the lower the compressive strength and the bond strength between the mortar and bricks.

Table 2 Similarity constant of the masonry structure model

| Type | Physical index | Dimension | Research model scale |
|----------------------|----------------------------------|-----------|----------------------|
| Material properties | Stress σ (Pa) | FL^{-2} | 1 |
| | Strain ϵ | – | 1 |
| | Young’s modulus E (Pa) | FL^{-2} | 1 |
| | Poisson’s ratio ν | – | 1 |
| | Mass density ρ (kg/m^3) | FL^{-3} | 10 |
| Geometric characters | Length l (m) | L | 1/10 |
| | Linear movement δ (m) | L | 1/10 |
| | Angular movement θ (rad) | – | 1 |
| | Area A (m^2) | L^2 | 1/100 |
| Load | Concentrated load P (N) | F | 1/100 |
| | Moment M (N m) | FL | 1/1000 |
| Dynamism characters | Mass m (kg) | F | 1/100 |

Table 3 Compressive strength and splitting tensile strength test results for footing concrete

| No | Mix (C:S:G:W) | Age (d) | Size (mm) | Compressive strength (MPa) | Splitting tensile strength (MPa) |
|----|---------------|---------|-------------|----------------------------|----------------------------------|
| 1 | 1:1.6:3.2:0.5 | 3 | 100×100×100 | 12.4 | 1.01 |
| 2 | | 7 | | 20.5 | 1.85 |
| 3 | | 28 | | 28.3 | 2.25 |

Table 4 Compressive strength test results for mortar

| No | Mix (C:S:W) | Age (d) | Size (mm) | Compressive strength (MPa) |
|----|--------------|---------|----------------|----------------------------|
| 1 | 210:1500:330 | 7 | 70.7×70.7×70.7 | 1.6 |
| 2 | 240:1500:330 | | | 1.7 |
| 3 | 260:1500:330 | | | 2.7 |
| 4 | 300:1500:330 | | | 3.1 |
| 5 | 400:1500:330 | | | 6.8 |
| 1 | 210:1500:330 | 14 | 70.7×70.7×70.7 | 2.2 |
| 2 | 240:1500:330 | | | 2.7 |
| 3 | 260:1500:330 | | | 4.2 |
| 4 | 300:1500:330 | | | 5.5 |
| 5 | 400:1500:330 | | | 9.5 |
| 1 | 210:1500:330 | 28 | 70.7×70.7×70.7 | 2.3 |
| 2 | 240:1500:330 | | | 3.5 |
| 3 | 260:1500:330 | | | 4.4 |
| 4 | 300:1500:330 | | | 5.5 |
| 5 | 400:1500:330 | | | 9.4 |

The wall thickness of masonry structures in the area is generally between 240 and 360 mm (Ministry of Housing and Urban–Rural Development of PRC 2011). The model is at one tenth scale, therefore the wall thickness of the model was set at 30 mm (Fig. 4). This required that the masonry model was built placing the bricks on their edge. Given the contact between bricks had a small contact area, a relatively high-strength mortar was adopted within the typical proportions of water, cement, and sand. The design specification for masonry mortar mix proportion (Ministry of Housing and Urban–Rural Development of PRC 2010) for a mix of 400:1500:330 (cement: sand: water) was chosen. The mortar test cubes cured for 28 days had an average compressive strength 9.4 MPa. When constructing walls, recommended practices such as soaking bricks in water, and dry mixing of mortar before adding water, were followed (Bothara et al. 2010). After constructed, the model was not tested until after 34 days. Figure 5 shows a view of the test model completed.

3.4 Loading protocol

The testing program was basically aimed at two objectives: (1) Investigating how masonry structure deformation is affected by the development of landslide tension cracks; and (2) Identifying the loading limits (e.g., speeds, total displacement) for wall

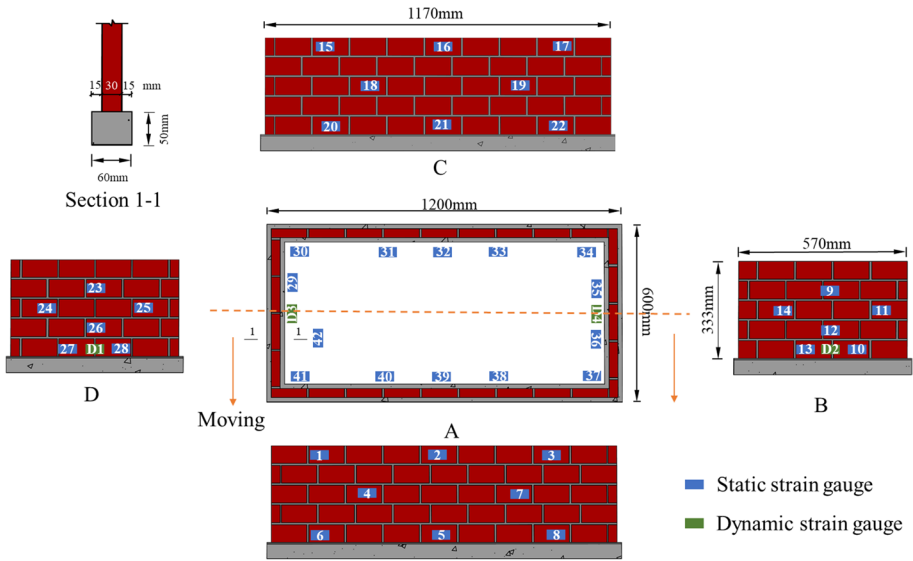


Fig. 4 Model plan (Walls A and C are longitudinal wall; Walls B and D are transverse walls)

The geometric scale of $s_l = 1/10$

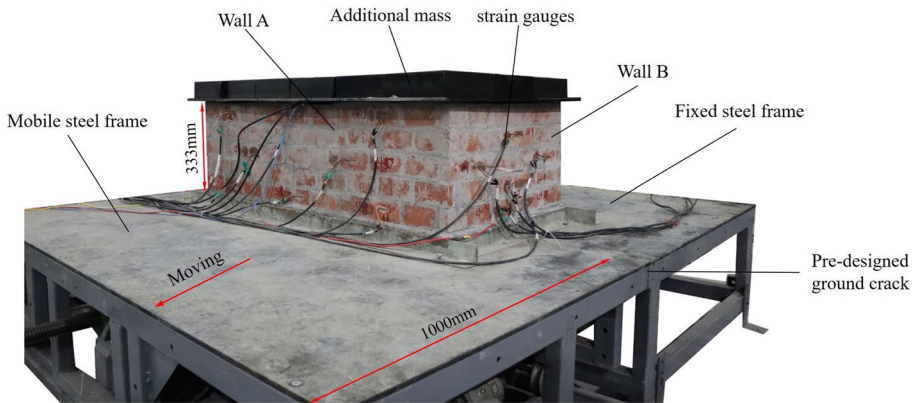


Fig. 5 View of the completed model

cracking. To investigate the model building’s response to the development of a landslide tension crack, the foundation of the model building was subjected to frequency-scaled landslide ground motion in the direction of tension (Fig. 6).

An initial tensile loading force of 0.84 kN is applied on the mobile frame for setup and the mobile frame is pulled in increments, applying tensile loads step-wise. Each loading force increase is 0.26 kN and is applied for 60 s. The test is stopped when cracks are observed in the walls of the model.

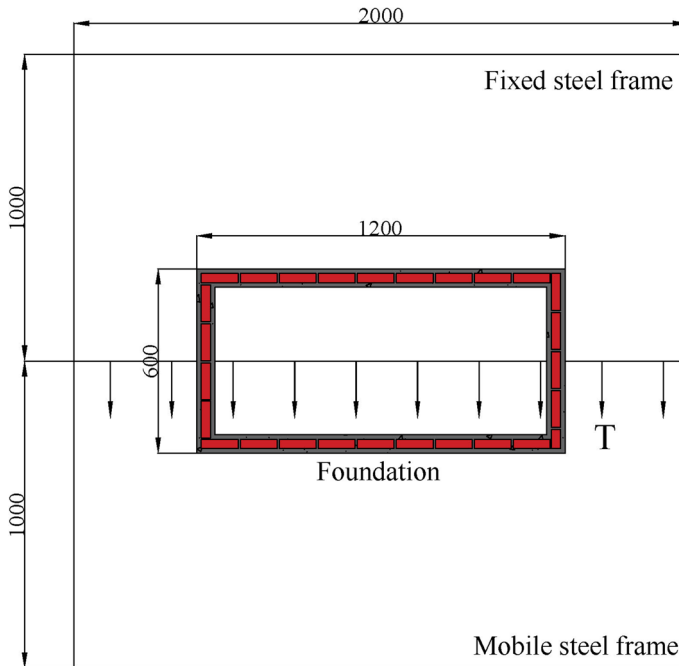


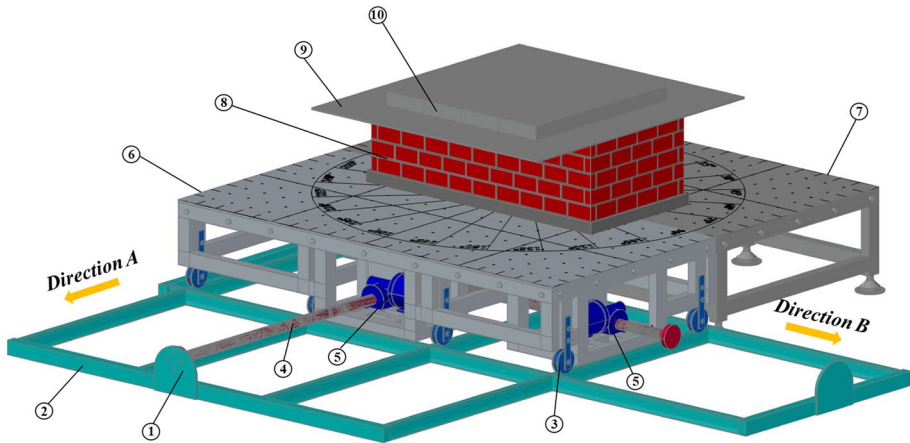
Fig. 6 Tension pattern of the model building's foundation (unit: mm; the "T" denotes the tractive force from the loading device)

4 Experiment setup and instrumentation

4.1 Loading device

Physical model devices have aimed at analyzing the response of a masonry structures subject to earthquake or tunnelling-induced settlements (Chung et al. 1988; Paolucci et al. 2008; Shi 2011; Graziotti et al. 2017; Giardina et al. 2012; Son and Cording 2005). However, these don't meet the requirements for simulating the process of masonry structures damaged by landslide surface tensile deformation.

The experimental loading device we designed consists of two steel frames (one fixed and one mobile), a drive system that consists of the electronic machinery and a reducer device, a roller, and a rail (Fig. 7). Table 5 shows the characteristics of the loading device. The mobile frame can move along direction A or B. In direction A, the model will be under tension or compression at its base. In direction B, the model will be under shear. The drive system is made up of the electric machinery, lead screw, and reaction frame. In order to control the moving speed of the mobile frame accurately, the frequency of the reducer to change the rotation speed of the screw can be adjusted. The tractive force corresponding to each frequency was calculated according to the parameters of the loading device in Table 5. Figure 8 shows the corresponding relationship between the moving speed and the tractive force of the mobile frame and the frequency of the reducer. The speed, the tractive force, and frequency have a linear correlation. A patent application has been filed for this device (the patent No. ZL 201910793347.9).



① Reaction frame ② Rail ③ Roller ④ Lead screw ⑤ Electric machinery ⑥ Fixed steel frame
 ⑦ Mobile steel frame ⑧ The model building ⑨ Load-bearing steel plate ⑩ Additional mass

Fig. 7 Diagram of the loading device

Table 5 Characteristics of the loading device

| Parameter | Value |
|------------------------|--|
| Size | 2000 mm × 2000 mm |
| Output | 1.5 kW |
| Voltage | 220 V |
| Moving speed (no load) | 0–10 mm/s |
| Frequency range | 0–50 Hz |
| Moving distance range | Direction A: 0–50 cm; Direction B: 0–100 cm |
| Force range | 0–12.5 kN |

4.2 Monitoring device and data processing

Strain gauges were placed on the wall and foundation to monitor their deformation in detail and back calculate the internal forces developed. A total of 42 static strain gauges (collecting data twice per second) and 4 dynamic strain gauges (collecting data 5000 times per second) were installed. The strain gauges were arranged with a higher density at the areas assessed as having the higher potential for developing cracks (Fig. 4).

The resistance of the strain gauges is 120 Ω, and their sensitivity coefficient is 2.0 ± 1%. The resistance of these sensors varies with deformation, and therefore changes in resistance caused by structure deformations at the location where the strain gauge is located can be converted into local strains. A static strain acquisition system with 64 channels (DH3816N) and a dynamic strain acquisition system with 8 channels (DH5921) were used to collect the strain data (produced by DONGHUA Company <http://www.dhtest.com/>).

Data processing was completed for static and dynamic strain gauges separately. For static strain gauges, peak values were used to analyze the strain response of the masonry

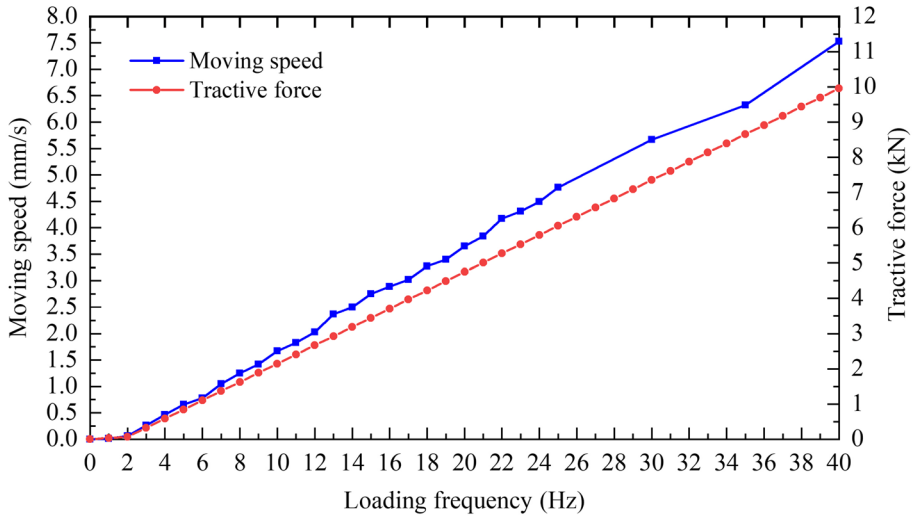


Fig. 8 Relationship between the moving speed and the tractive force of the mobile frame in Direction A

wall. For dynamic strain gauges, we apply the low-pass filter to denoise and chose 35 Hz as the cutoff frequency (Zhang et al. 2016b). Then, data subsampling was performed to 100 values per second. The data generated were used to analyze the transient changes of strain when the walls are cracking under the extension imposed by the mobile plate through the foundation.

Video cameras were set up opposite to the four walls to record the deformation process of the model building. Combining with video and strain monitoring results, the loading time of cracking in the model can be accurately obtained, which helps to analyze the relationship between the loading force and the deformation of the model.

5 Results

5.1 Strain response

During the displacement of the mobile frame at step-wise loading increments, a maximum force of 5.26 kN is reached, at which the model then became severely damaged. The peak tensile forces of the static strain gauges at each stage are shown in Figs. 9 and 10.

As shown in Fig. 9a, the strain values associated with each loading increment measured by the static strain gauges in Wall B appear stable and between 0 and $5 \mu\epsilon$. Strain then increased sharply as the loading force approaches 5.26 kN (the strain measured by Strain Gauge 12 increased to $27,628.74 \mu\epsilon$ in the last step). The sudden strain increase corresponds to the nature of the stress-controlled test as opposed to strain-controlled and identifies the moment of wall cracking at the location of the strain gauge. The strain measured by Strain Gauge 10 increased from 0.19 to $43.94 \mu\epsilon$, and the value of the Strain Gauge 11 from 2.12 to $43.3 \mu\epsilon$. The increase in strain measured by other strain gauges is relatively small in comparison. These suggest the internal force in wall B

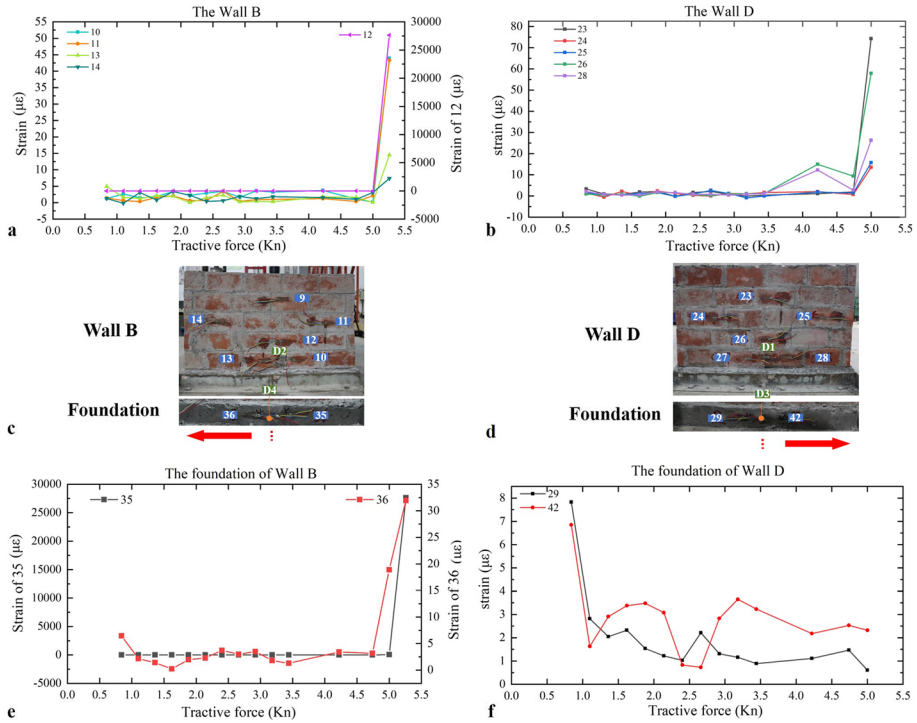


Fig. 9 Measured static strains and locations of static strain gauges on the transverse walls and their foundation. **a** strain response of Wall B; **b** strain response of Wall D; **c** location of strain gauges on Wall B and its foundation; **d** location of strain gauges on Wall D and its foundation; **e** strain response of the foundation of Wall B; **f** strain response of the foundation of Wall D

changed dramatically at a loading force of 5.26 kN, eventually cracking under the external load imposed by the displacement of the mobile frame.

Figure 9b presents the change in measured strain in Wall D during the test and against the applied force at each step. Up to 4.22 kN, the monitoring strain values in Wall D were also stable. It is observed that the values measured by Strain Gauge 26 and 28 rose about 10 µε for an applied load of 4.22 kN. This indicates that Wall D was subjected to tension at this moment of the test that led to internal forces that are enough to initiate small cracking and fissures (noticed during detail inspection of the video recordings); however, the remaining strength is sufficient to resist the external force and the wall had no large cracking development. When the loading force was 5.00 kN, all strain values increased suddenly, especially Strain Gauge 23 and 26, which are located in the middle of the wall. The measured strain value at Strain Gauge 23 increased from 1.92 to 74.26 µε and the value at Strain Gauge 11 increased from 9.32 to 57.87 µε.

Figure 9e shows that the strains measured at the foundations of Wall B had a similar behavior as those strains measured for the wall. The strain measured by Strain Gauge 35 increased to 27,614.72 µε suddenly, indicating the time of cracking. It is noted from Fig. 9f, that the measured strain values at Strain Gauge 29 and 42 in the foundation of Wall D were between 0 and 8 µε. These changes are very small compared to the other

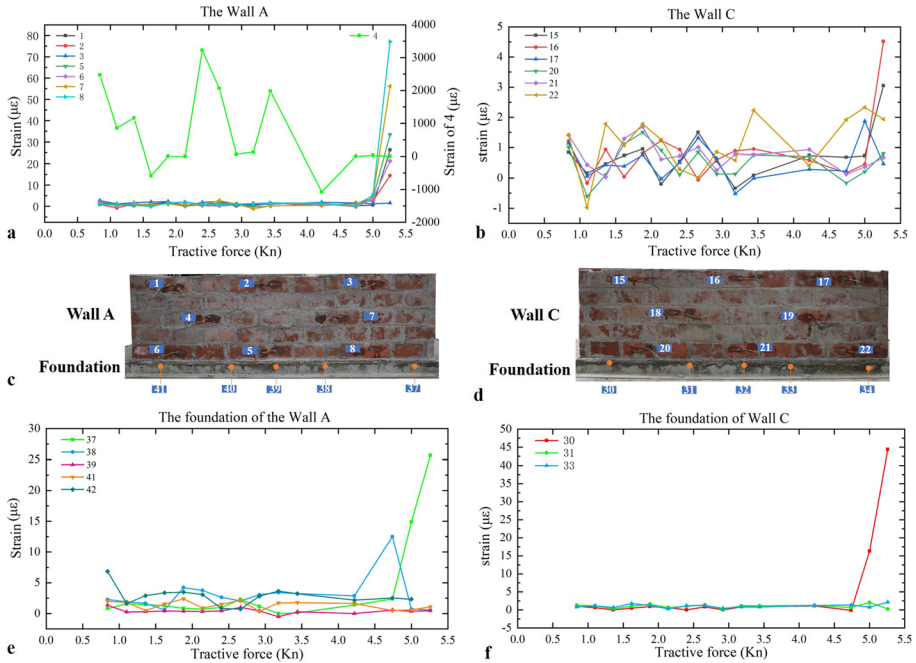


Fig. 10 Measured static strains and locations of static strain gauges on the longitudinal walls and their foundation. **a** Strain response of Wall A; **b** strain response of Wall C; **c** location of static strain gauges on Wall A and its foundation; **d** location of static strain gauges on Wall C and its foundation; **e** strain response of the foundation of Wall A; **f** strain response of the foundation of Wall C

observations, indicating that the cracking developed in an area not fully captured by the position of the strain gauges.

Figure 10a shows that the measured strains in Wall A prior to the load step of 5.26 kN were stable except for Strain Gauge 4. The measured strains in all other strain gauges had a similar response to those in Wall B and Wall D, greatly increasing at the 5.26 kN step. This indicates that the macro-cracks initiated on Wall A at this final step. Strains measured at the strain gauges on Wall C ranged between -1 and $5 \mu\epsilon$ during the whole loading process (Fig. 10b). No macro-cracks were observed on this wall at that stage.

Figure 10e and f presents the measured strain response of strain changes at the foundations of Wall A and Wall C. The strain values were stable during the test except for the strain measurements at Strain Gauge 37 and 30. The strains at Strain Gauge 37 and 30 increased significantly during the last two stages of the test to maximum values of $25.66 \mu\epsilon$ and $44.4 \mu\epsilon$, respectively. These two strain gauges were placed near each corner of the foundation.

5.2 Strain response during wall cracking

When the loading force transmitted through the mobile frame reached 5.00 kN, the measured strain at the strain gauge in the foundation of Wall D increased to $125.52 \mu\epsilon$ after 23 s of the loading being set (Fig. 11). This suggested the progressive cracking of the foundation at the position of the dynamic strain gauge D3 (See Fig. 9c). Once the

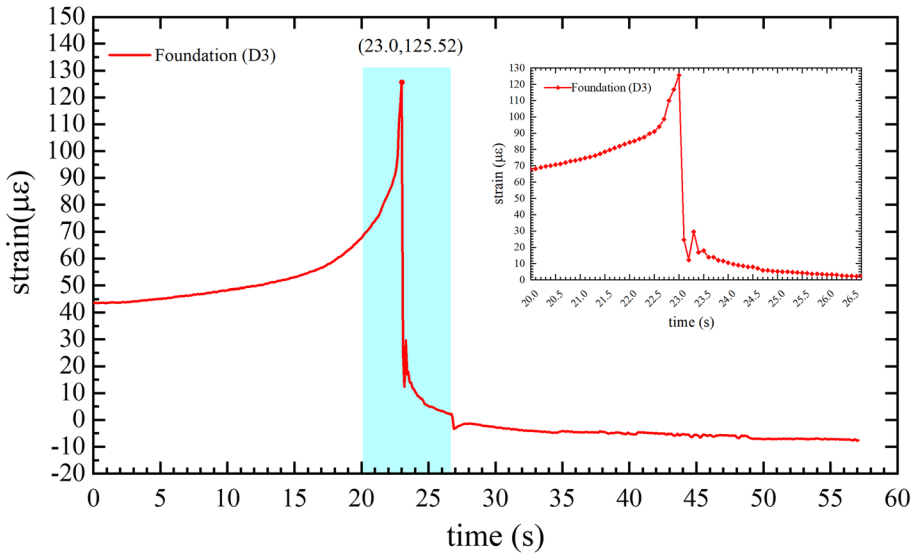


Fig. 11 Dynamic strain measured at the foundation of Wall D during cracking at the stage associated with a loading force of 5.00 kN

foundation collapses through cracking at a different location, the strain measured at D3 decreased rapidly due to a relief in the internal stress. It is noted that the strain recovery is total.

Wall B and its foundation began cracking at the stage associated with a force of 5.26 kN. Observations during the test identified that the foundation was damaged first, and then cracks appeared on the wall. Figure 12 shows the time elapsed between

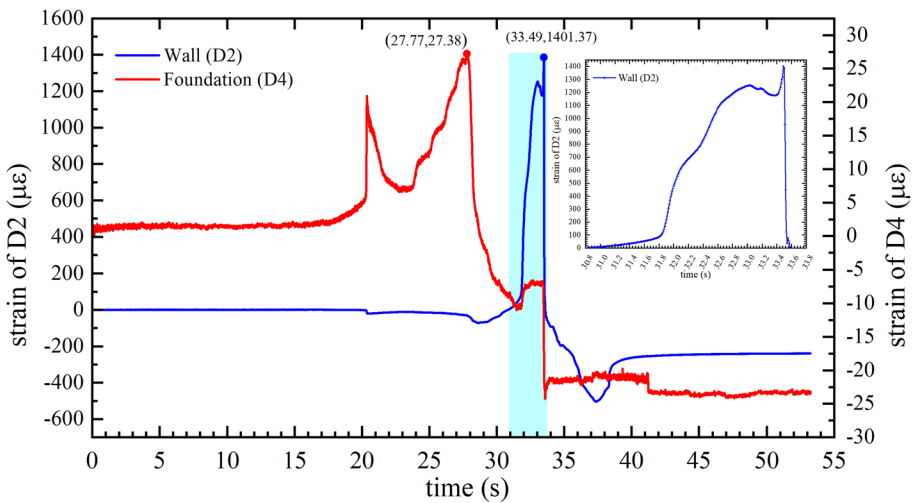


Fig. 12 Dynamic strain measured at Wall B and its foundation during cracking at the stage associated with a loading force of 5.26 kN

foundation and wall cracking was 5.72 s. The maximum measured strain of the wall was $1401.37 \mu\epsilon$. Strains decreased rapidly after the foundation and wall crack significantly.

5.3 Visual observations

Wall B cracked at 34 s after application of the stage associated with a loading force of 5.26 kN (Fig. 13a and c). The crack was observed to increase with the sustained load. At first, the crack appeared on the foundation of Wall B, and then extended to the wall itself.

Foundation D cracked 23 s after application of the stage associated with a loading force of 5.00 kN. However, there was no obvious crack evolution with sustained loading. This suggests the overall reminding strength is greater than the tension applied through the mobile steel frame. At the stage associated with a loading force of 5.26 kN, the crack width was increased and it extended to the corner of the wall, at the connection with Wall A (Fig. 13 b and d). A diagonal crack of 45° was formed in wall D along the mortar joints (Fig. 14a). Another diagonal crack extended from the corner where the wall meets Wall D and to the top of the Wall A at an angle of 45° and along the mortar joints (Fig. 14b). As shown in Fig. 15, the crack in the foundation was 30 mm distant from the simulated ground crack. A vertical crack formed on the wall from bottom to top, and along the brick and mortar joint.

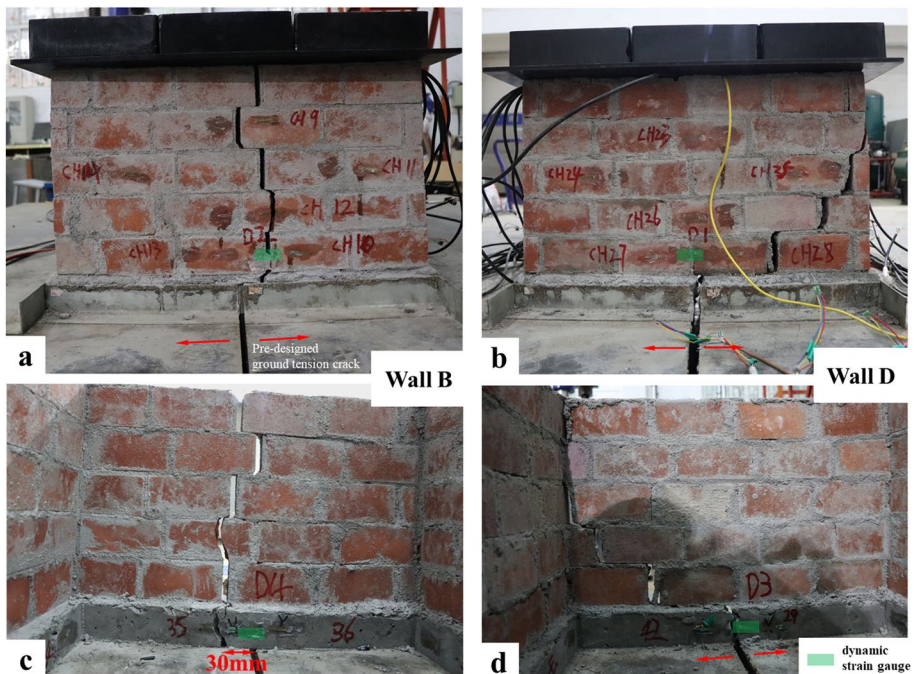


Fig. 13 Distribution of cracks on Wall B and Wall D. **a** outer surface of Wall B; **b** outer surface of Wall D; **c** internal surface of wall B; **d** internal surface of wall D

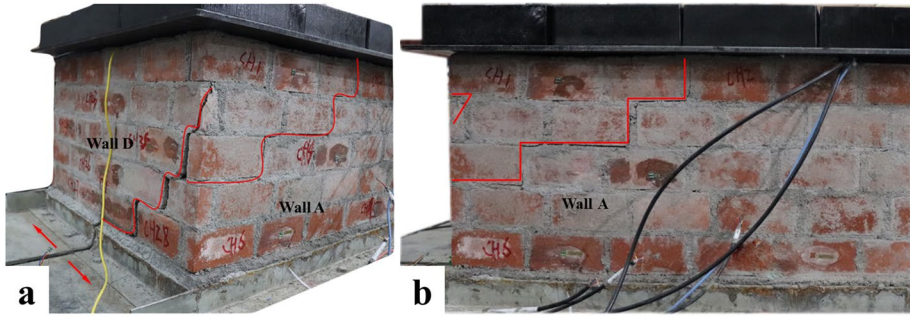


Fig. 14 Distribution of cracks on Wall A and Wall D. **a** Crack at the corner between the Wall A and Wall D; **b** cracks on Wall A

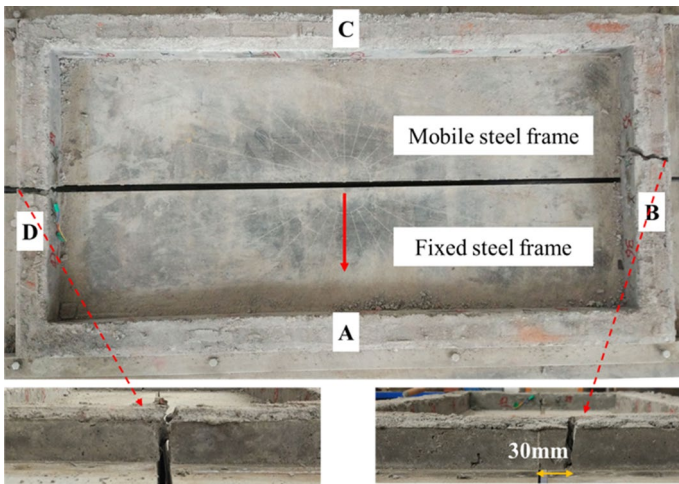


Fig. 15 Cracks at the foundation

6 Discussion

Scarce information is available to empirically estimate or predict the vulnerability of buildings threatened by ground deformations on slow-moving landslides. Through the experiments presented here, the damage process of the masonry structure affected can be observed and monitored by the dynamic evolution of the landslide from deformation to failure.

6.1 Validations

To validate the experiment, the results were compared with the field investigations and published observation. Validations were made from horizontal movement building movement, and building damage patterns.



Fig. 16 The crack pattern of the masonry buildings. **a** The photograph was taken by May 2019, in the Shengjibao landslide. **b** The picture was referred by Antronico et al. (2015). The masonry building located in the Cemetery area, Italy was damaged by the slow-moving landslide. **c** The picture was referred by Somma et al. (2020). The masonry building due to its low tensile strength showed separation of brick–mortar joints

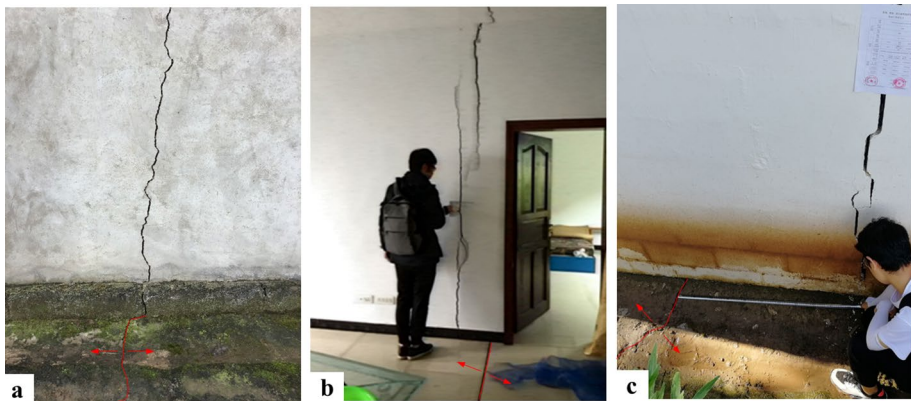


Fig. 17 The wall crack patterns and the ground surface cracks on the slow-moving landslides. **a** and **b** The photographs were taken by January 2019, in the Tangjiao landslide. **c** The photograph was taken by July 2020, in the Lipingcun landslide

Common characteristics include that wall cracking mostly occurs in proximity of the location where the surface tension crack develops in the ground, and that wall corners show to be very fragile. The diagonal crack along the mortar joints usually appears on the corner of the wall, which seriously compromises the structure integrity and further movement is likely to lead to a total collapse. This damage characteristic is verified by the filed observation and some literatures (Antronico et al. 2015; Somma et al. 2020) as shown Fig. 16. Due to the weak tensile resistance of the masonry structure, when the masonry structure is damaged under the ground tension cracks, the wall cracks are easy to appear on the bottom of the wall and then extend to the wall corner, along the mortar joint with an angle of 30° or 45° . Meanwhile, when the wall across the ground cracks, the vertical cracks generally appear in the wall and extend from the bottom to top of the wall. Figure 17 shows the wall crack patterns and the ground surface cracks on the slow-moving landslides which is similar to the experimental results (Fig. 13a and c).

Visual observations of the damage to the scaled model after the test revealed the same response to those observed for structures damaged by slow-moving landslides. Therefore,

the test results are reliable and reveal the evolution of failure of the masonry structures affected by the tension cracks on the slow-moving landslides.

6.2 A threshold exists on the damage of buildings on slow-moving landslide

Buildings on slow-moving landslides have their own resistance. However, they will experience cracking once the resistance is exceeded. During step-by-step loading process in the test, the increase in strains were generally smooth and of very small magnitude. When the loading force reaches to 5.00 kN and 5.26 kN, the strains of transverse walls which were across the tension ground crack increased significantly as the wall developed substantial damage (full-scale crack). This indicates that for landslide-generated stresses lower than the structure strength, little deformation and cracking is generated on the structure. If the intensity of landslide reaches the resistance of the building, the wall damage increases exponentially (brittle response). This can also explain the differences in the damage observed on buildings built on a same landslide, due to spatial difference in intensity of the landslide (Alexander 1989; Bianchini et al. 2015).

6.3 The damage patterns of the masonry structure and the ground tension crack on the slow-moving landslide

The wall on the sliding body is more susceptible to damage than the wall on the stable ground. The two longitudinal walls which were not on the ground tension crack had different levels of damage. Wall A was damaged, but Wall C was safe. The reason can be because Wall A was located on the mobile steel frame and Wall C was located on the fixed steel frame. The wall located on the sliding body suffers severer damage if the building across a tension crack.

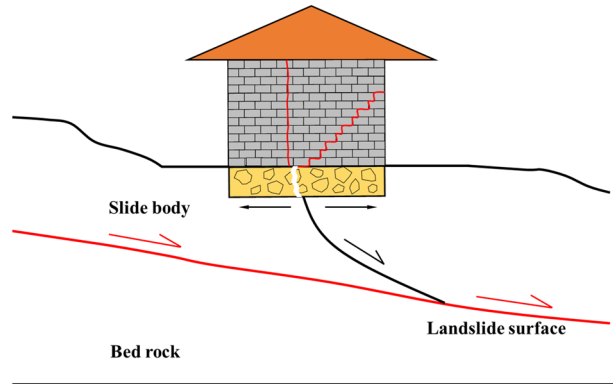
Therefore, through the analysis of masonry buildings affected by the tension cracks on the slow-moving landslides, the characteristics of ground cracks and building damage can be described:

- (1) Buildings affected by tensile deformation are usually located at the crown or the toe of the landslide. These places are prone to transverse ground cracks in the rock and soil mass under gravity due to external factors. When the ground crack passes through the wall of the masonry buildings, it causes damage to the structure.
- (2) Because masonry structures have weak tensile resistance, when they are subjected to surface tensile deformation, the buildings are prone to oblique cracks extending from bottom to top along the mortar joints at 30° – 60° toward the wall corners.
- (3) When the ground crack goes through the wall, the wall usually develops vertical cracks extending from bottom to top through the wall. The floor, walls, and junctions between walls of the building appear cracks with basically the same width up and down, as shown in Fig. 18.

6.4 Future research potential and risk control suggestions in terms of increasing the resistance of buildings on slow moving landslide

After the physical model test was completed, the masonry structure model of the test was simulated by the finite element software Abaqus. Under the same loading conditions as

Fig. 18 The damage pattern of the masonry building affected by the tension crack on the slow-moving landslide



the test, the simulation obtained the equivalent plastic strain and crack distribution of the model, as shown in Fig. 19a. A vertical crack appeared in the middle of the wall and extended upward from the bottom of the foundation to the top of the wall. The model damaged patterns of the numerical simulation are basically consistent with the experimental results. As shown in Fig. 19b, it shows the stress distribution of the wall with spanning the ground tension crack. The Mises equivalent stress is represented by stress contour to show the stress distribution of the model, which can quickly determine the most dangerous area in the model. The foundation and bottom of the model wall are under tension, which is basically consistent with the experimental results.

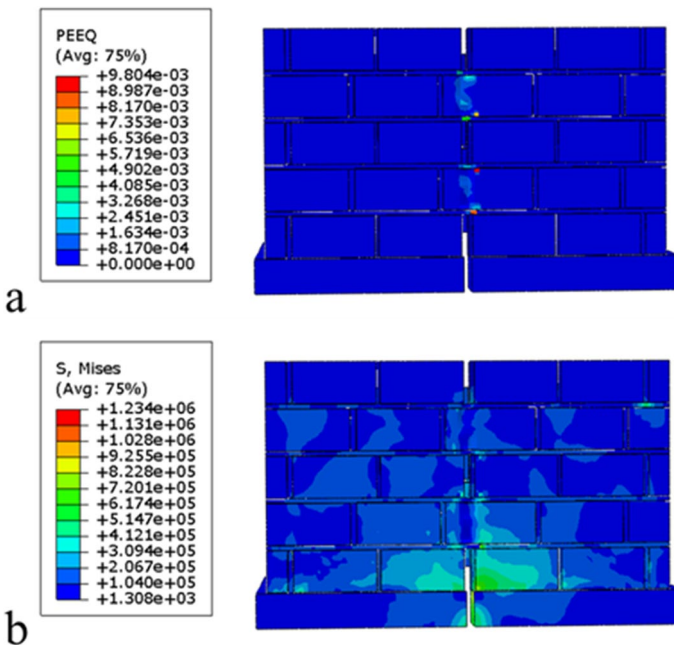


Fig. 19 The numerical simulation results. **a** The equivalent plastic strain distribution of the test model wall. **b** Mises equivalent stress distribution of the test model

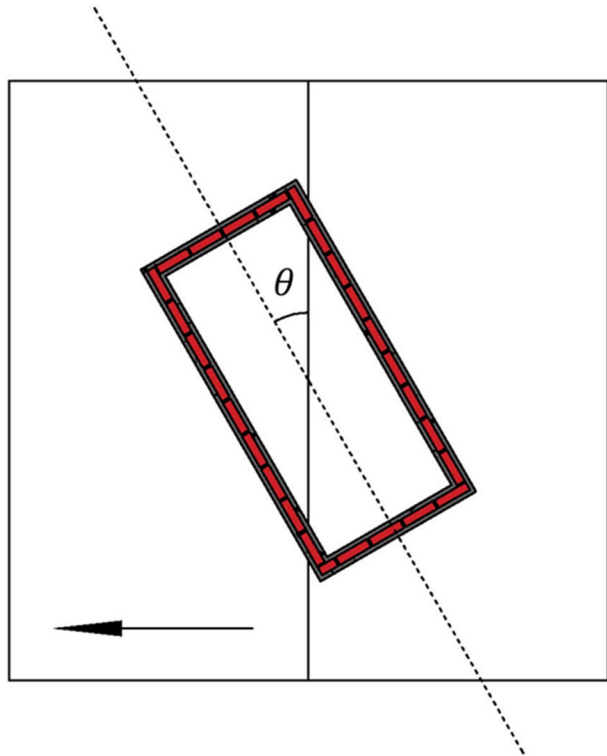
In the future research, numerical simulation methods can be used to analyze and compare the structural failure threshold when the building is located with different angles between the axial line of the building and the ground cracks (Fig. 20). Meanwhile, the sensitivity analysis of the physical vulnerability of the building can be performed by changing the load state (shear, compression) or moving speeds of landslides.

This experimental method opens the opportunity to, through increased testing and observations, develop reasonable and practical strength indices of building damage and landslide activity to establish the vulnerability curve of masonry structures affected by slow-moving landslides based on the field observations and experimental data.

Meanwhile, the results of the experiment suggest that brittle failure of these structures under landslide-induced ground tension cracks. Increasing the ductility of the structures through implementation of reinforced masonry construction methods and reinforcement of the wall corners could be implemented to provide more structural stability and warning of impending collapse to residents.

Finally, many landslides are caused by earthquakes in mountainous areas. The seismic frequency content is an important characteristic of seismic ground motion (Esmaeilabadi et al. 2015) and has a significant impact on structural damage. In the future research, for landslides caused by seismic activity, the damage influence of different frequency contents on landslide and buildings can be considered.

Fig. 20 The different loading angle of the masonry model



6.5 Limitations

- (1) The actual building is built the foundation soils. But in this test, the model was built on the experimental steel plate. It assumes that the experimental table is the sliding body of landslide.
- (2) Due to the limitation of the size of the experiment setup, a one-tenth model was designed. The size of the test brick is the smallest which the factory can produce. To meet the wall thickness scale of 1/10, a different brick layout was used than those in full size buildings (laid on their thinner side for the scaled model -stretcher- as opposed to their wide side) (Fig. 21). This can affect the overall stiffness of the structure.
- (3) To reduce construction and interpretation complexity, we didn't make the partition walls, and doors, and windows. The resistance of the model would be greater if the wall density of the structure increases.
- (4) From the visual observations of the test, it found that the two transverse walls didn't suffer extensive damaged at the same time. Wall D was significantly damaged for a loading force of 5.00 kN and Wall B at 5.26 kN. Possible reasons include small variations in material properties and the construction of the scale model, or any uneven loading under the two walls. An 8-mm gap was identified between the mobile steel frame and the fixed steel frame close to the location where Wall D was placed, no gap on the other side was identified. Although the system is reset before the test, this gap could explain the different loads at which the walls failed.

7 Conclusion

To better understanding the damaging effect and the mechanism of the buildings across tension cracks on slow-moving landslides, an experimental investigation and obtain some meaningful findings are presented.

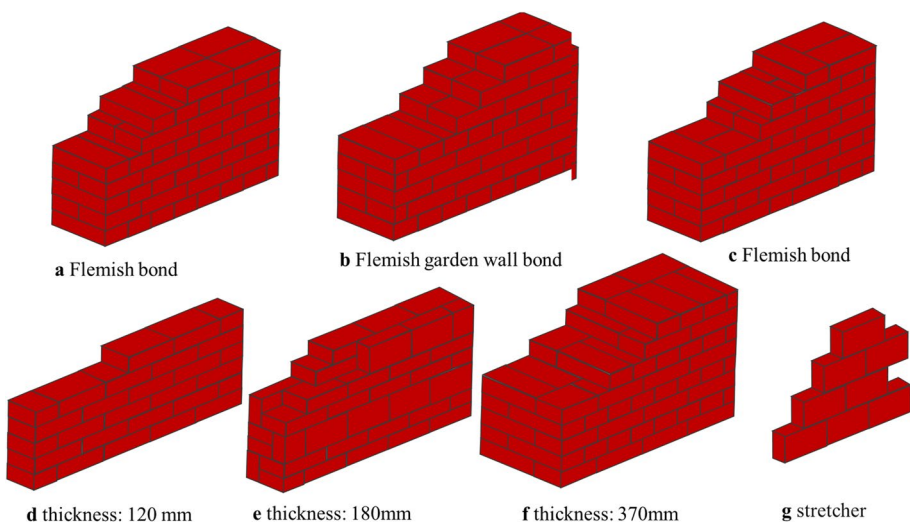


Fig. 21 Masonry construction methods

The experiment presented in this study successfully modeled the damage process of buildings across tension cracks on a slow-moving landslide. It consists of two main parts: the one-tenth scale model of a masonry building and the loading device. The masonry model is built with concrete strip footing, scaled bricks, and mortar. The experiment loading device consists of two steel plates, each attached to a frame (one fixed and one mobile), a drive system, rollers, and rails. The moving speed of the mobile frame is controlled accurately by the drive system consisting of two electric machineries, two lead screws, and tow reducers. The contact surface between the mobile steel frame and the fixed steel frame is used as a ground crack on a slow-moving landslide. When the drive system is started, the model on the steel plates will be under tension. The newly developed experimental loading device can simulate building damage caused by ground horizontal displacements and can bridge the gap in understanding the effects of slow-moving landslides on structures.

There is a force threshold of landslide loading on the building. Damaged buildings on the slow-moving landslide experience a process from resistance to cracking. In this research, the strains of the walls did not present an increasing trend with the gradual increase of the loading force but the strain of the walls had a sudden increase when the internal strength of the wall was reached (brittle behavior). After initial large-scale cracking of the wall, the progressive opening of the landslide ground crack will determine the degree of damage to the building. The model building was severely damaged when the loading force was 5.26 kN, with very limited deformation measured at lower loads but for the initial development of some fissures on the foundation and walls in the model. In terms of physical vulnerability quantification, the results suggest that when the landslide intensity is lower than the building resistance, the building structure would show no signs of significant distress and the vulnerability value would be zero. The starting point of a vulnerability curve for buildings on slow-moving landslides should be the threshold of landslide loading on the building.

For a slow-moving landslide, the local ground displacement and location of ground surface cracks are the direct cause of damage to masonry structures. According to the strain changes of the walls and the location of macroscopic cracks, the foundation near the ground crack is the most susceptible to damage. Compared to the walls that did not cross the ground cracks, the walls that crossed the ground cracks were severely damaged. Furthermore, the corner of the walls also shows to concentrate structure stresses which are reflected in excessive damage.

Although limitation exists, the test results provide a new way to analyze the vulnerability of masonry structure across tension cracks on slow-moving landslides.

Acknowledgements We thank Xinghua Zhu, Juting Zhang, Wenfang Zhang, and other laboratory colleagues for assisting to complete the physical model test. We want to thank the editors and the two anonymous reviewers for their constructive comments, which helped us to improve the quality of the article.

Author contributions All authors contributed to the study conception and design. LC and LG designed the physical model test plan. The test material preparation, data collection, and field work were performed by QC, YZ and YL. And QC carried out the analysis of the test data. KY and LC supervised the research. The first draft of the manuscript was written by QC, and all authors commented on previous versions of the manuscript. RM and LC revised and improved this manuscript. All authors read and approved the final manuscript.

Funding This research is supported by two projects “Studies on spatial–temporal differences in large accumulation landslide deformation and its vulnerability model for buildings in the Three Gorges reservoir” (Grant No. 41877525) and “Study on the dynamic response of the quantitative vulnerability of buildings in different evolution stages of landslides” (Grant No. 41601563), both of which are financed by the National Natural Science Foundation of China. The first author (Grant No. 202106410017) is supported by China

Scholarship Council (CSC) as a visiting Ph.D. student at the University of Alberta, Canada, under Dr. Renato Macciotta's supervision.

Data availability The data of material strength and the model strain were our original data by test. The data of landslide displacement and building damaged were collected by the field work. And the monitoring data of the Xiangjiaping Landslides was provided by the Geological Environment Monitoring Master Station of Chongqing. The data are not available online. If readers want to have the data, they can request it by e-mail from the authors.

Declarations

Conflict of interest The authors declare that they have no known competing financial interests or personal relationships that could have appeared to influence the work reported in this paper.

References

- Alexander D (1989) Urban landslides. An international review of geographical work in the natural and environmental sciences. *Prog Phys Geogr* 13:157–191
- Ali R, Kuriqi A, Kisi O (2020) Human-environment natural disasters interconnection in China: a review. *Climate* 8:1–28. <https://doi.org/10.3390/cli8040048>
- Antronico L, Borrelli L, Coscarelli R, Gullà G (2015) Time evolution of landslide damages to buildings: the case study of Lungro (Calabria, southern Italy). *Bull Eng Geol Environ* 74:47–59. <https://doi.org/10.1007/s10064-014-0591-y>
- Bianchini S, Ciampalini A, Raspini F, Bardi F, Di Traglia F, Moretti S, Casagli N (2015) Multi-temporal evaluation of landslide movements and impacts on buildings in San Fratello (Italy) by means of C-Band and X-Band PSI data. *Pure Appl Geophys* 172:3043–3065. <https://doi.org/10.1007/s00024-014-0839-2>
- Bothara JK, Dhakal RP, Mander JB (2010) Seismic performance of an unreinforced masonry building: an experimental investigation. *Earthq Eng Struct Dyn* 39:45–68. <https://doi.org/10.1002/eqe.932>
- Buckingham E (1914) On physically similar systems; Illustrations of the use of dimensional equations. *Phys Rev* 4:345–376. <https://doi.org/10.1103/PhysRev.4.345>
- Carlà T, Macciotta R, Hendry M, Martin CD, Edwards T, Evans T, Farina P, Intrieri E, Casagli N (2018) Displacement of a landslide retaining wall and application of an enhanced failure forecasting approach. *Landslides* 15:489–505. <https://doi.org/10.1007/s10346-017-0887-7>
- Cascini L, Fornaro G, Peduto D (2010) Advanced low- and full-resolution DInSAR map generation for slow-moving landslide analysis at different scales. *Eng Geol* 112:29–42. <https://doi.org/10.1016/j.enggeo.2010.01.003>
- Chen Q, Chen L, Gui L, Yin K, Shrestha DP, Du J, Cao X (2020) Assessment of the physical vulnerability of buildings affected by slow-moving landslides. *Nat Hazards Earth Syst Sci* 20:2547–2565. <https://doi.org/10.5194/nhess-20-2547-2020>
- Chen L, Cao X, Yin K, Wu Y, Li Y (2016) Physical vulnerability assessment for buildings impacted by a slow moving landslide based on field work and statistical modelling. In: *Proceeding of 12th international symposium on landslides*, vol 2, Napoli, Italy, 2016, pp 627–634. <https://doi.org/10.1201/b21520-70>
- Chung LL, Reinhorn AM, Soong TT (1988) Experiments on active control of seismic structures. *J Eng Mech* 114:241–256. [https://doi.org/10.1061/\(ASCE\)0733-9399\(1988\)114:2\(241\)](https://doi.org/10.1061/(ASCE)0733-9399(1988)114:2(241))
- Cruden DM, Varnes DJ (1996) Landslide types and processes. In: Turner AK, Schuster RL (eds) *Landslides, investigation and mitigation Special Report 247*. Transportation Research Board, National Research Council, vol 3. National Academy Press, Washington, pp 36–75
- Deane E, Macciotta R, Hendry MT, Gräpel C, Skirrow R (2020) Leveraging historical aerial photographs and digital photogrammetry techniques for landslide investigation—a practical perspective. *Landslides* 17:1989–1996. <https://doi.org/10.1007/s10346-020-01437-z>
- Du F, Xu M, Xiao X, Ning N (2018) Physical simulation modeling for stability analysis of reservoir landslide in gently underdip slopes: a case study of Xiangjiaping landslide. *J Eng Geol* 26:694–702. <https://doi.org/10.13544/j.cnki.jeg.2017-175>

- Du J, Yin K, Glade T, Woldai T, Chai B, Xiao L, Wang Y (2020) Probabilistic hazard analysis of impulse waves generated by multiple subaerial landslides and its application to Wu Gorge in Three Gorges Reservoir, China. *Eng Geol* 276:105773. <https://doi.org/10.1016/j.enggeo.2020.105773>
- Esmailabadi R, Abasszadeh Shahri A, Behzadafshar K, Gheirati A, Nosrati Nasrabadi J (2015) Frequency content analysis of the probable earthquake in Kopet Dagh region—Northeast of Iran. *Arab J Geosci* 8:3833–3844. <https://doi.org/10.1007/s12517-014-1446-3>
- Fell R (2018) Human induced landslides. Landslides and engineered slopes. Experience, theory and practice, pp 171–199
- Ferlisi S, Gullà G, Nicodemo G, Peduto D (2019) A multi-scale methodological approach for slow-moving landslide risk mitigation in urban areas, southern Italy. *Euro-Mediterr J Environ Integr* 4:20. <https://doi.org/10.1007/s41207-019-0110-4>
- Ferlisi S, Marchese A, Peduto D (2021) Quantitative analysis of the risk to road networks exposed to slow-moving landslides: a case study in the Campania region (southern Italy). *Landslides* 18:303–319. <https://doi.org/10.1007/s10346-020-01482-8>
- Ferlisi S, Peduto D, Gullà G, Nicodemo G, Borrelli L, Fornaro G (2015) The use of DInSAR data for the analysis of building damage induced by slow-moving landslides. In: Lollino G et al. (eds) *Engineering geology for society and territory—volume 2: Landslide processes*. Springer Nature, Switzerland, pp 1835–1839. <https://doi.org/10.1007/978-3-319-09057-3>
- Galli M, Guzzetti F (2007) Landslide vulnerability criteria: a case study from Umbria, central Italy. *Environ Manage* 40:649–664. <https://doi.org/10.1007/s00267-006-0325-4>
- Giardina G, Marini A, Hendriks MAN, Rots JG, Rizzardini F, Giuriani E (2012) Experimental analysis of a masonry façade subject to tunnelling-induced settlement. *Eng Struct* 45:421–434. <https://doi.org/10.1016/j.engstruct.2012.06.042>
- Graziotti F, Tomassetti U, Kallioras S, Penna A, Magenes G (2017) Shaking table test on a full scale URM cavity wall building. *Bull Earthq Eng* 15:5329–5364. <https://doi.org/10.1007/s10518-017-0185-8>
- Guo Z, Chen L, Yin K, Shrestha DP, Zhang L (2020) Quantitative risk assessment of slow-moving landslides from the viewpoint of decision-making: a case study of the Three Gorges Reservoir in China. *Eng Geol* 273:105667. <https://doi.org/10.1016/j.enggeo.2020.105667>
- Huntley D, Bobrowsky P, Hendry M, Macciotta R, Elwood D, Sattler K, Best M, Chambers J, Meldrum P (2019) Application of multi-dimensional electrical resistivity tomography datasets to investigate a very slow-moving landslide near Ashcroft, British Columbia, Canada. *Landslides* 16:1033–1042. <https://doi.org/10.1007/s10346-019-01147-1>
- Jiang H, Li Y, Zhou C, Hong H, Glade T, Yin K (2020) Landslide displacement prediction combining LSTM and SVR algorithms: a case study of shengjibao landslide from the three gorges reservoir area. *Appl Sci (Switzerland)* 10:1–21. <https://doi.org/10.3390/app10217830>
- Journault J, Macciotta R, Hendry MT, Charbonneau F, Huntley D, Bobrowsky PT (2018) Measuring displacements of the Thompson River valley landslides, south of Ashcroft, BC, Canada, using satellite InSAR. *Landslides* 15:621–636. <https://doi.org/10.1007/s10346-017-0900-1>
- Kang H, Kim Y (2016) The physical vulnerability of different types of building structure to debris flow events. *Nat Hazards* 80:1475–1493. <https://doi.org/10.1007/s11069-015-2032-z>
- Kilicoglu C, Cetin M, Aricak B, Sevik H (2020) Site selection by using the multi-criteria technique—a case study of Bafra, Turkey. *Environ Monit Assess* 192:608. <https://doi.org/10.1007/s10661-020-08562-1>
- Li Y, Utili S, Milledge D, Chen L, Yin K (2021) Chasing a complete understanding of the failure mechanisms and potential hazards of the slow moving Liangshuijing landslide. *Eng Geol* 281:105977. <https://doi.org/10.1016/j.enggeo.2020.105977>
- Liang X, Gui L, Wang W, Du J, Ma F, Yin K (2021) Characterizing the development pattern of a colluvial landslide based on long-term monitoring in the three gorges reservoir. *Remote Sens* 13:1–23. <https://doi.org/10.3390/rs13020224>
- Liu S, Segoni S, Raspini F, Yin K, Zhou C, Zhang Y, Casagli N (2020) Satellite InSAR as a new tool for the verification of landslide engineering remedial works at the Regional Scale: a case study in the three gorges Reservoir area, China. *Appl Sci* 10:6435. <https://doi.org/10.3390/app10186435>
- Lowry B, Gomez F, Zhou W, Mooney MA, Held B, Grasmick J (2013) High resolution displacement monitoring of a slow velocity landslide using ground based radar interferometry. *Eng Geol* 166:160–169. <https://doi.org/10.1016/j.enggeo.2013.07.007>
- Macciotta R, Hendry M, Martin CD (2016) Developing an early warning system for a very slow landslide based on displacement monitoring. *Nat Hazards* 81:887–907. <https://doi.org/10.1007/s11069-015-2110-2>
- Macciotta R, Carlà T, Hendry M, Evans T, Edwards T, Farina P, Casagli N (2017) The 10-Mile slide and response of a retaining wall to its continuous deformation Renato, advancing culture of living with landslides. Springer International Publishing, Cham. <https://doi.org/10.1007/978-3-319-53487-9>

- Mansour MF, Morgenstern NR, Martin CD (2011) Expected damage from displacement of slow-moving slides. *Landslides* 8:117–131. <https://doi.org/10.1007/s10346-010-0227-7>
- Mansour MF (2009) Characteristic behaviour of slow-moving slides. Ph.D. Thesis, University of Alberta
- Mavrouli O, Corominas J, Ibarbia I, Alonso N, Jugo I, Ruiz J, Luzuriaga S, Navarro JA (2019) Integrated risk assessment due to slope instabilities in the roadway network of Gipuzkoa, Basque Country. *Nat Hazards Earth Syst Sci* 19:399–419. <https://doi.org/10.5194/nhess-19-399-2019>
- Ministry of Housing and Urban–Rural Development of PRC (2011) Code for design of masonry structures. China Architecture and Building Press, Beijing
- Ministry of Housing and Urban–Rural Development of the PRC (2009) Standard for test method of performance on building mortar. China Architecture and Building Press, Beijing
- Ministry of Housing and Urban–Rural Development of the PRC (2010) Specification for mix proportion design of masonry mortar. China Architecture and Building Press, Beijing
- Ministry of Housing and Urban–Rural Development of the PRC (2019) Standard for test methods of concrete physical and mechanical properties. China Architecture and Building Press, Beijing
- Nicodemo G, Ferlisi S, Peduto D, Aceto L, Gullà G (2020) Damage to masonry buildings interacting with slow-moving landslides: a numerical analysis. In: Calvetti F, Cotecchia F, Galli A, Jommi C (eds) *Geotechnical research for land protection and development CNRIG 2019. Lecture Notes in Civil Engineering*, vol 40. Springer, Cham. https://doi.org/10.1007/978-3-030-21359-6_6
- Paolucci R, Shirato M, Yilmaz MT (2008) Seismic behaviour of shallow foundations: Shaking table experiments vs numerical modelling. *Earthq Eng Struct Dyn* 37:577–595. <https://doi.org/10.1002/eqe.773>
- Peduto D, Ferlisi S, Nicodemo G, Reale D, Pisciotta G, Gullà G (2017) Empirical fragility and vulnerability curves for buildings exposed to slow-moving landslides at medium and large scales. *Landslides* 14:1993–2007. <https://doi.org/10.1007/s10346-017-0826-7>
- Rodriguez J, Deane E, Hendry MT, Macciotta R, Evans T, Gräpel C, Skirrow R (2021) Practical evaluation of single-frequency dGNSS for monitoring slow-moving landslides. *Landslides* 18:3671–3684. <https://doi.org/10.1007/s10346-021-01737-y>
- Sangirardi M, Amorosi A, de Felice G (2020) A coupled structural and geotechnical assessment of the effects of a landslide on an ancient monastery in Central Italy. *Eng Struct* 225:111249. <https://doi.org/10.1016/j.engstruct.2020.111249>
- Shahri AA, Spross J, Johansson F, Larsson S (2019) Landslide susceptibility hazard map in southwest Sweden using artificial neural network. *Catena* 183:104225. <https://doi.org/10.1016/j.catena.2019.104225>
- Shi Y (2011) Study on the base damage mechanics of bridge and building under ground fissure with large-scale tests. Ph.D. Thesis, Chang'an University.
- Singh A, Kanungo DP, Pal S (2019) Physical vulnerability assessment of buildings exposed to landslides in India. *Nat Hazards* 96:753–790. <https://doi.org/10.1007/s11069-018-03568-y>
- Somma F, Millen M, Bilotta E, Flora A, Viana Da Fonseca A (2020) Vulnerability assessment of RC buildings to lateral spreading. *Bull Earthq Eng* 18:3629–3657. <https://doi.org/10.1007/s10518-020-00847-7>
- Son M, Cording EJ (2005) Estimation of building damage due to excavation-induced ground movements. *J Geotech Geoenviron Eng* 131:162–177. [https://doi.org/10.1061/\(asce\)1090-0241\(2005\)131:2\(162\)](https://doi.org/10.1061/(asce)1090-0241(2005)131:2(162))
- Sun Q, Zhang L, Ding X, Hu J, Liang H (2015) Investigation of slow-moving landslides from ALOS/PAL-SAR images with TcPInSAR: a case study of Oso, USA. *Remote Sens* 7:72–88. <https://doi.org/10.3390/rs70100072>
- Uzielli M, Catani F, Tofani V, Casagli N (2015) Risk analysis for the Ancona landslide—II: estimation of risk to buildings. *Landslides* 12:83–100. <https://doi.org/10.1007/s10346-014-0477-x>
- Woods A, Hendry MT, Macciotta R, Stewart T, Marsh J (2020) GB-InSAR monitoring of vegetated and snow-covered slopes in remote mountainous environments. *Landslides* 17:1713–1726. <https://doi.org/10.1007/s10346-020-01408-4>
- Woods A, Macciotta R, Hendry MT, Stewart T, Marsh J (2021) Updated understanding of the deformation characteristics of the Checkerboard Creek rock slope through GB-InSAR monitoring. *Eng Geol* 281:105974. <https://doi.org/10.1016/j.enggeo.2020.105974>
- Wu Y, Liu DS, Li MJ (2011) landslide model experiment for energy dissipation law in sliding and impact processes. *Chin J Rock Mech Eng* 30:693–701
- Xu Q, Tang MG, Xu KX, Huang XB (2008) Research on space-time evolution laws and early warning-prediction of landslides. *Chin J Rock Mech Eng* 27:1104–1112
- Yang B, Yin K, Lacasse S, Liu Z (2019) Time series analysis and long short-term memory neural network to predict landslide displacement. *Landslides* 16:677–694. <https://doi.org/10.1007/s10346-018-01127-x>

- Yu B, Yi W, Zhao H (2018) Experimental study on the maximum impact force by rock fall. *Landslides* 15:233–242. <https://doi.org/10.1007/s10346-017-0876-x>
- Zhang J, Guo ZX, Wang D, Qian H (2016a) The quantitative estimation of the vulnerability of brick and concrete wall impacted by an experimental boulder. *Nat Hazards Earth Syst Sci* 16:299–309. <https://doi.org/10.5194/nhess-16-299-2016>
- Zhang J, Zhai X, Liu B, Jiang W (2016) Analysis and processing of strain measurement data of solid rocket motor. *Meas Control Technol* 35:36–39. <https://doi.org/10.19708/j.ckjs.2016.09.009>
- Zhou C, Cao Y, Yin K, Wang Y, Shi X, Catani F, Ahmed B (2020) Landslide characterization applying sentinel-1 images and InSAR technique: The Muyubao landslide in the three Gorges Reservoir area. *China Remote Sens* 12:3385. <https://doi.org/10.3390/rs12203385>

Publisher's Note Springer Nature remains neutral with regard to jurisdictional claims in published maps and institutional affiliations.

Springer Nature or its licensor (e.g. a society or other partner) holds exclusive rights to this article under a publishing agreement with the author(s) or other rightsholder(s); author self-archiving of the accepted manuscript version of this article is solely governed by the terms of such publishing agreement and applicable law.

Authors and Affiliations

Qin Chen^{1,2} · Lixia Chen³  · Renato Macciotta² · Kunlong Yin¹ · Lei Gui¹ · Yu Zhao³ · Yingxue Liao³

✉ Lixia Chen
lixiaichen@cug.edu.cn

Qin Chen
chengzi@cug.edu.cn

Renato Macciotta
macciott@ualberta.ca

Kunlong Yin
yinkl@cug.edu.cn

Lei Gui
lei.gui@cug.edu.cn

Yu Zhao
cugzhaoyu@cug.edu.cn

Yingxue Liao
yingxueliao@cug.edu.cn

¹ Faculty of Engineering, China University of Geosciences, Wuhan 430074, China

² Department of Civil and Environmental Engineering, University of Alberta, Edmonton, AB T6G 1H9, Canada

³ Institute of Geophysics and Geomatics, China University of Geosciences, No. 388, Lumo Road, Hongshan District, Wuhan 430074, Hubei, China